Computing Magnetic Noise With Micro-Magneto-Mechanical Simulations

Christian Dorn and Stephan Wulfinghoff

Institute for Materials Science—Computational Materials Science, Kiel University, 24143 Kiel, Germany

We study magnetic noise caused by the interaction of domain walls with defects. In the first step, we formulate a micro-magneto-mechanical material model using the generalized standard materials framework. We use this model in the subsequent step, in which we devise a scheme to compute magnetic noise based on ensemble averaging. We demonstrate our approach with numerical examples using the finite element method.

Index Terms— **Coupled problem, ensemble averaging, finite element method, magnetic noise.**

I. Introduction

HIGH performance magnetic field sensors are required for detecting biomagnetic fields of the heart and brain. Superconducting quantum interference devices are the current standard for magneto-encephalography and -cardiography. However, high technical complexity and operating expenses limit access to these diagnostic facilities. Hence, it is desirable to develop easy-to-use and inexpensive alternative sensor concepts, see [1]. Further improvement of sensor performance requires noise reduction (especially magnetic noise). To this end, we want to model, simulate, and understand magnetic noise in magnetostrictive thin-film composites. Different noise origins can be subsumed as magnetic noise and there are different approaches to study magnetic noise. Thermal magnetization fluctuations have been investigated by experimental [2], analytical [3] and computational [4] approaches. Furthermore, noise due to magnetic domain wall jumps at pinning sites [5], [6], [7] (Barkhausen noise) has been studied in the past. Here we are interested in the latter. We set up a micro-magneto-mechanical material model and apply it to compute magnetic noise.

II. Modeling and Simulation of Micro-Magneto-Mechanical Material

We consider a micro-magneto-mechanical film V_{mag} on a mechanical substrate V_{mech} embedded in a free space box Ω, such that $V_{\text{mag}} \cup V_{\text{mech}} = V \supset \Omega$, see Fig. 1. For the time range, we write $[0, \tau]$. The coupled problem is characterized by the following fields: displacement $\boldsymbol{u} : V \times [0, \tau] \to \mathbb{R}^3$, scalar magnetic potential $\varphi : \Omega \times [0, \tau] \to \mathbb{R}$ and magnetization $\boldsymbol{m} : V_{\text{mag}} \times [0, \tau] \to \mathcal{S}^2$. Here we denote by $\mathcal{S}^2$ the unit sphere in $\mathbb{R}^3$. The material behavior is determined by potential optimization. We include the following contributions.

1) Exchange energy $\Psi_{\text{ex}}(\nabla \boldsymbol{m}) = \int_V A \, \|\nabla \boldsymbol{m}\|^2 dV$.
2) Anisotropy energy $\Psi_a(\boldsymbol{m}) = \int_V K_1 \big(1 - (\boldsymbol{m} \cdot \boldsymbol{e}_a)^2\big) dV$.

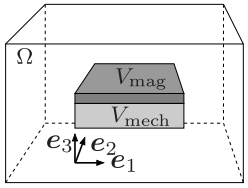

Fig. 1. Magneto-mechanical film V_{mag} on mechanical substrate V_{mech} embedded in free space box Ω.

3) Demagnetizing energy $\Psi_d(\boldsymbol{m}, \nabla\varphi) = \int_V \mu_0 \nabla\varphi \cdot M_s \boldsymbol{m} dV - (1/2) \int_\Omega \mu_0 \|\nabla\varphi\|^2 dV$ with demagnetizing field $\boldsymbol{H}_d = -\nabla\varphi$.
4) Zeeman energy $\Psi_z(\boldsymbol{m}) = \int_V -\mu_0 M_s \boldsymbol{m} \cdot \boldsymbol{H}' dV$ with externally applied field $\boldsymbol{H}'$.
5) Elastic energy $\Psi_{\text{el}}(\boldsymbol{\varepsilon}, \boldsymbol{m}) = \int_V (1/2)\, \boldsymbol{\varepsilon}^e : \mathbb{C} : \boldsymbol{\varepsilon}^e dV$ with small strain setting and additive strain decomposition $\boldsymbol{\varepsilon} = \text{sym}(\text{grad}(\boldsymbol{u})) = \boldsymbol{\varepsilon}^e + \boldsymbol{\varepsilon}^{\text{m}}$ and magnetostrictive strain $\boldsymbol{\varepsilon}^{\text{m}} = (3/2)\lambda_s (\boldsymbol{m} \otimes \boldsymbol{m} - (1/3)\boldsymbol{I})$.
6) Dissipation potential $\Phi(\dot{\boldsymbol{m}}) = \int_V (\eta/2) \dot{\boldsymbol{m}} \cdot \dot{\boldsymbol{m}} dV$.

$\mathbb{C}$ denotes the stiffness tensor (here isotropic) and $\boldsymbol{\varepsilon}^e$ denotes the elastic part of the strain tensor $\boldsymbol{\varepsilon}$. This formulation of the elastic energy implies linear elasticity. Besides the (conservative) energy contributions, we also incorporate the potential Φ to reflect the dissipative nature of magnetization changes. For details on dissipation potential and the associated generalized standard material approach see [8], [9]. The material parameters for the magneto-mechanical film (FeCoSiB) and substrate are summarized in Table I. All energies and the dissipation potential contribute to the rate potential

$$\Pi = \dot{\Psi}_{\text{ex}} + \dot{\Psi}_{\text{el}} + \dot{\Psi}_a + \dot{\Psi}_d + \dot{\Psi}_z + \Phi \tag{1}$$

which we intend to optimize (constrained optimization, $\|\boldsymbol{m}\| = 1$). To account for this constraint we use exponential mapping [9], [10]. To optimize the time-discrete rate potential Π, we compute the stationary points with respect to the degrees of freedom $\boldsymbol{u}$, $\boldsymbol{m}$ and φ. The stationary points subsequently serve as residuals for the global Newton–Raphson scheme.

To obtain results without boundary effects (e.g., without closure domains) we use periodic boundary conditions (pbc). Our implementation relies on the idea to adapt the mesh files such that the periodic nodes have the same node numbers, see [11]. With pbc, we represent an infinitely extended

Manuscript received 21 June 2022; revised 12 September 2022; accepted 21 September 2022. Date of publication 6 October 2022; date of current version 26 January 2023. Corresponding author: C. Dorn (e-mail: cdo@tf.uni-kiel.de).

Color versions of one or more figures in this article are available at https://doi.org/10.1109/TMAG.2022.3212764.

Digital Object Identifier 10.1109/TMAG.2022.3212764

TABLE I
MATERIAL PARAMETERS (ESTIMATED)

		FeCoSiB	substrate
A	exchange constant	$1.5 \cdot 10^{-11}\,\frac{\mathrm{J}}{\mathrm{m}}$	–
M_s	spontaneous magnetization	$1.5 \cdot 10^{6}\,\frac{\mathrm{A}}{\mathrm{m}}$	–
K_1	anisotropy constant	$3 \cdot 10^{2}\,\frac{\mathrm{J}}{\mathrm{m}^3}$	–
$\boldsymbol{e}_\mathrm{a}$	easy axis	$\boldsymbol{e}_1$	–
η	viscosity parameter	$1 \cdot 10^{-5}\,\frac{\mathrm{J\cdot s}}{\mathrm{m}^3}$	–
λ_s	saturation magnetostriction	$30 \cdot 10^{-6}$	–
λ	first Lamé parameter	172GPa	150GPa
μ	second Lamé parameter	54GPa	50GPa

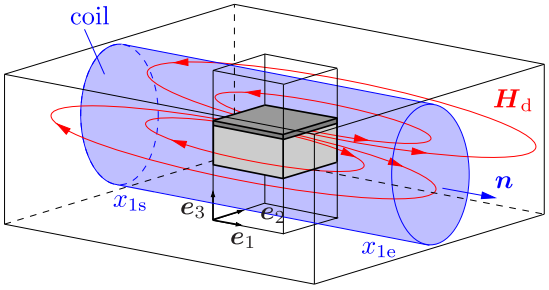

Fig. 2. Stack of *free space—film—substrate—free space* with pbc in $\boldsymbol{e}_1$- and $\boldsymbol{e}_2$-direction (central column) embedded in surrounding free space, continuous coil with normal $\boldsymbol{n}$ to pick up demagnetizing field $\boldsymbol{H}_d$.

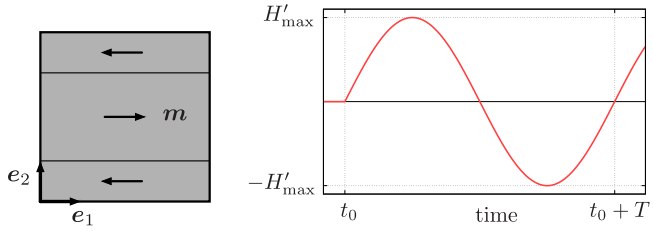

(a) (b)

Fig. 3. (a) Sketch of initialization of magnetization $\boldsymbol{m}(\boldsymbol{x}, 0)$ in magneto-mechanical film. (b) Loading function $H'(t)$ for applied field $\boldsymbol{H}' = H'(t)\boldsymbol{e}_1$ with $t_0 = 10^{-9}$ s, $T = 3 \cdot 10^{-7}$ s and $H'_\mathrm{max} = 10^{-2}$ A/μm.

material. However, we still intend to have the material embedded in free space (for reasons explained below). To marry the two approaches we devise the following workflow. In a precursory simulation we solve the fully coupled problem for the stack of *free space—film—substrate—free space* with pbc in $\boldsymbol{e}_1$- and $\boldsymbol{e}_2$-direction (central column in Fig. 2). During this simulation we record the time history of magnetization $\boldsymbol{m}(\boldsymbol{x}, t)$. In a subsequent simulation on the full computational domain (central column embedded in surrounding free space) we use the recorded magnetization history $\boldsymbol{m}(\boldsymbol{x}, t)$ and only solve for magnetic potential φ. The result is the material behavior of an infinitely extended material, which is still embedded in free space and still creates the corresponding demagnetizing field. The idea of this approach is to approximately model a small fraction of a *huge* composite (much too large for numerical resolution) and its contribution to the overall magnetic noise.

For the investigation of magnetic noise, we are interested in the interaction of domain walls with defects. To this end, we require well-defined and controllable domain walls.

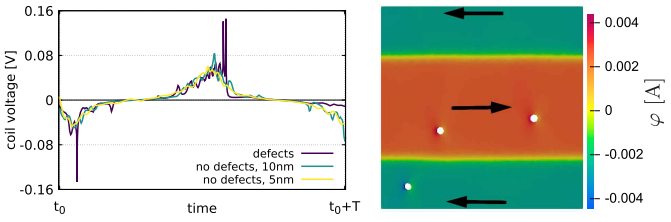

(a) (b)

Fig. 4. (a) Induced coil voltage over time with and without defects (mesh sizes 5 and 10 nm). (b) Relaxed state at $t \approx t_0$ for corresponding microstructure with three cylindrical holes, displayed: φ and $\boldsymbol{m}$ (at three significant locations).

The initialization of magnetization $\boldsymbol{m}(\boldsymbol{x}, 0)$ in Fig. 3(a) is compatible with the pbc at hand and yields two domain walls which can be controlled by the applied field $\boldsymbol{H}'(t)$ in $\boldsymbol{e}_1$-direction. To decrease the time to reach initial equilibrium (relaxation time), we prescribe the transition of magnetization between neighboring domains in a continuous fashion (similar to Néel wall). After relaxation we apply a sinusoidal external magnetic field $\boldsymbol{H}' = H'(t)\boldsymbol{e}_1$, see Fig. 3(b). This results in a reciprocating domain wall motion and repeated interaction with defects.

To study noise, we have to specify a signal. The signal is motivated by the working principle of the magnetoelectric thin-film sensor in [1]. The demagnetizing field $\boldsymbol{H}_d$ emitted by the magnetic material is picked up by a coil, see Fig. 2. The coil voltage (average-induced electromotive force) serves as the signal. For a discrete coil, consisting of N loops at positions x_i, each with area $A(x_i)$, the coil voltage $\overline{U}$ reads

$$\overline{U} = \frac{1}{N} \sum_{i=1}^{N} \left[- \int_{A(x_i)} \frac{d\boldsymbol{B}}{dt} \cdot \boldsymbol{n} dA \right]. \tag{2}$$

In the limit $N \to \infty$ we obtain an integral over the (continuous) coil volume

$$\overline{U} = -\frac{1}{L} \int_{x_{1s}}^{x_{1e}} \int_{A} \frac{d\boldsymbol{B}}{dt} \cdot \boldsymbol{n} dA dx_1 = -\frac{1}{L} \int_{V_\mathrm{coil}} \frac{d\boldsymbol{B}}{dt} \cdot \boldsymbol{n} dV \tag{3}$$

see Fig. 2. The quantity in (3) serves as signal for the noise investigation in Sections III and IV.

We solve the micro-magneto-mechanical problem using the finite element method. We rely on ParFEAP 8.6.1j (MPI parallel version of FEAP [12]) together with PETSc 3.13.2 [13]. We discretize space with tetrahedral elements and use linear shape functions for the fields of interest. Time derivatives are discretized by a finite difference scheme.

III. NOISE COMPUTATION BY ENSEMBLE AVERAGING

The magnetic noise that we investigate is caused by the interaction of domain walls with defects. To study this noise, we need to introduce prototypical defects. For simplicity, we consider three cylindrical holes with identical radii that penetrate the entire thickness of the magneto-mechanical film.

The interaction of domain wall and defect arises as follows. It is energetically favorable for domain walls to attach to defects (reduces e.g. exchange energy). Upon application of the applied field, the energy landscape changes, domain walls are forced away from defects and detach (given a sufficiently large

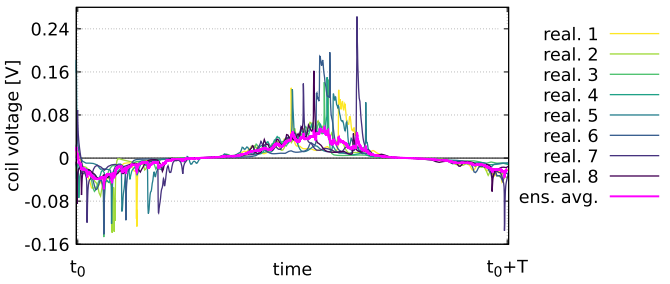

Fig. 5. Coil voltages over time for ensemble of eight realizations, ensemble average (ens. avg.).

applied field). An example of a coil voltage is displayed in Fig. 4(a) together with the voltage for a microstructure without defect (at mesh sizes 5 and 10 nm). The defect microstructure and corresponding local fields are shown in Fig. 4(b). The two large voltage peaks in Fig. 4(a) can correspond to events where a domain wall attaches, respectively, detaches from a defect (here: wall attaches). For the microstructure without defects we observe non-smooth behavior as well, which illustrates mesh influence. By comparison, however, the non-smoothness due to defect interactions dominates (see Section IV-B). The result in Fig. 4(a) applies to one realization of the microstructure i.e. to one specific geometrical placement of defects. For many different realizations with varying defect positions, the coil voltages are unique every time: coil voltage peaks take place at different times and exhibit various peak heights, see Fig. 5. We call this an *ensemble of microstructures*. The positions of the three cylindrical holes are chosen randomly and all positions within the magneto-mechanical film are equally likely. By introducing the ensemble we have transitioned from one tangible microstructure with three fixed defects to an abstract microstructure with a statistical distribution of three defects. For one realization we obtain a signal, see Fig. 4(a). For an ensemble of realizations, we obtain an average signal superposed by noise, see Fig. 5. We can view the magneto-mechanical problem as a system: the input is a microstructure; the output is a coil voltage. If we input a distribution of microstructures (ensemble) we obtain a distribution of coil voltages (average voltage and noise).

We consider M realizations. For each realization i we obtain coil voltage array u_i over time array t_i. Computation of noise voltage power spectral density $S_{\delta u}$ is based on

$$S_{\delta u}(f) = \lim_{T\to\infty} \left\langle \frac{|\widehat{\delta u_T}(f)|^2}{T} \right\rangle \tag{4}$$

where f is the frequency, T is the size of time range, $\langle\bullet\rangle$ denotes the ensemble average, δu is the fluctuation of coil voltage around the mean value, index T denotes truncated quantities and $\widehat{(\bullet)}$ denotes a Fourier transform, see [14]. For computational evaluation, we consider a finite time range only (omit limit, drop index T). We compute noise as follows.

1) Compute mean coil voltage (ensemble average) $\langle u\rangle = (1/M)\sum_{i=1}^{M} u_i$.
2) Compute coil voltage fluctuation for each realization $\delta u_i = u_i - \langle u\rangle$, $i = 1,\ldots,M$.
3) Compute Fourier transform of fluctuations $\widehat{\delta u_i} = \mathcal{FFT}(\delta u_i)$.

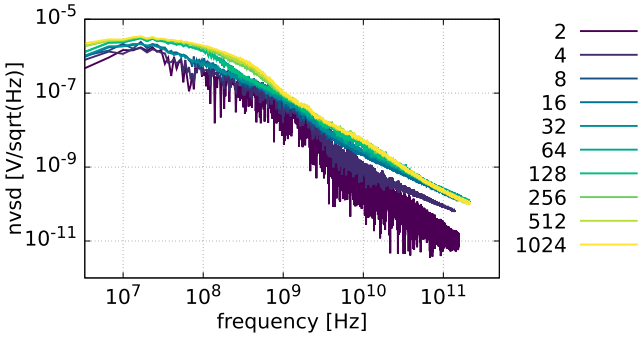

Fig. 6. Noise voltage spectral density for ensembles of different sizes.

4) Compute two-sided noise voltage power spectral density $S_{\delta u} = \Delta t^2((1/M)\sum_{i=1}^{M}(|\widehat{\delta u_i}|^2/T))$ where we need Δt^2 for consistency with the time continuous case.
5) Compute one-sided noise voltage spectral density (nvsd) $\text{nvsd} = \sqrt{2S_{\delta u}}$.

IV. Numerical Examples

A. Required Ensemble Size

In this first example, we study the required number of realizations in an ensemble to obtain a converged nvsd. To this end, we consider an ensemble with 1024 realizations. Each realization contains three cylindrical defects with radius 10 nm. Dimensions of the film are $0.5 \times 0.5 \times 0.01$ μm and dimensions of the substrate are $0.5 \times 0.5 \times 0.05$ μm. The free space box measures $2.5 \times 2.5 \times 2.06$ μm. We place defects in the film at least one defect radius away from the boundary to avoid conflict with pbc. For the random placement, we rely on the python function `random.uniform`. To compute noise we consider coil voltages over one sine-period of the applied field. The time range contains approximately $300 \cdot 10^3$ points which yields a time resolution of $\Delta t \approx 1$ ps. The one-sided nvsd for different ensemble sizes is displayed in Fig. 6. The smaller ensembles are subsets of the full 1024 ensemble. In Fig. 6 we observe that ensemble sizes 2 and 4 are too small since the noise spectra differ significantly from the 1024 ensemble. Remarkably, the noise spectrum of the ensemble with size 8 is very close to the full 1024 ensemble already. For the ensembles with more than or equal to 256 realizations the spectra (almost) coincide.

B. Influence of Mesh on Noise Spectrum

Next, we investigate the influence of spatial discretization. The mesh must be sufficiently fine to resolve domain walls, the width of which is determined by the exchange length [15]. In case of the soft-magnetic thin-films at hand the exchange length reads $l_{\text{ex}} = (2A/(\mu_0 M_s^2))^{1/2} \approx 3.26$ nm. We consider an ensemble of 8 realizations at three different resolutions (element size 9, 6 and 3 nm), see Fig. 7. The ensemble size of 8 offers a good compromise between computation effort and ensemble convergence, see Section IV-A. The rest of the setup for the numerical experiment is the same as in Section IV-A, except that the time resolution in this case is $\Delta t \approx 4$ ps. The nvsd for the three mesh resolutions is shown in Fig. 8. We observe that the spectra (almost) coincide. Hence it is not required to resolve the exchange length to obtain a physically

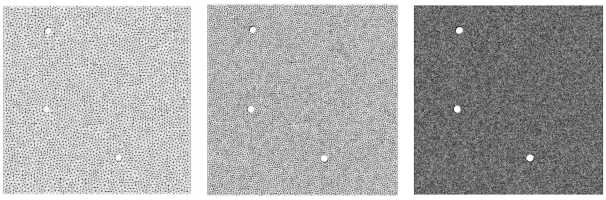

(a) (b) (c)

Fig. 7. Same realization with mesh sizes. (a) 9 nm. (b) 6 nm. (c) 3 nm.

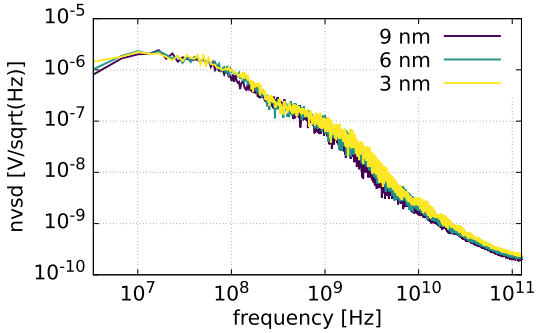

Fig. 8. Noise voltage spectral density for three different mesh sizes.

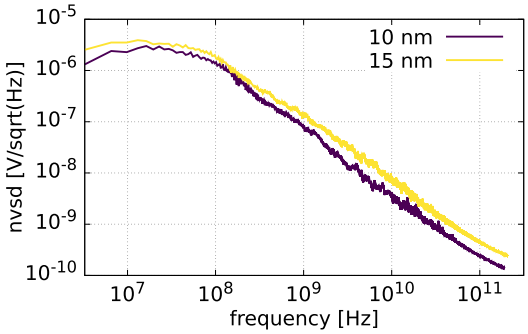

Fig. 9. Noise voltage spectral density for two different defect radii.

plausible noise spectrum. In the present case, mesh size $\approx 3l_{\text{ex}}$ appears to be sufficient.

C. Influence of Defect Radius on Noise Spectrum

In this last example, we study how defect variation affects noise. We compare the noise spectra of two ensembles (size 64) with different defect radii (10 and 15 nm). The specification of the ensembles is the same as in Section IV-A. With $190 \cdot 10^3$ time points we obtain a time resolution of $\Delta t \approx 1.6$ ps. In Fig. 9 the resulting nvsd for both defect radii is displayed. We observe that the larger defects cause greater noise at all frequencies. The following explanation appears plausible. Domain walls are more attracted to larger defects (greater energy gain). The larger attraction causes build-up of higher magnetic field to overcome the attraction which in turn leads to a higher energy release upon detaching. This results in higher coil voltage peaks and greater noise. In this explanation we assume that the field is sufficiently large for domain walls to overcome defects. If not, larger defects could even decrease noise by preventing domain walls detaching from defects.

This example illustrates that the presented noise computation scheme is sensitive to anticipated influence factors of magnetic noise. Thus this example gives a strong indication that the computed noise spectra are physically plausible.

V. Conclusion

In the present work, we have introduced a scheme to compute magnetic noise based on micro-magneto-mechanical simulations. The scheme exhibits desirable properties such as ensemble convergence, apparent mesh independence (within certain limits), and physical plausibility. In the future, we want to consider numerical examples where mechanics plays a more pronounced role. Furthermore, studying more realistic defects and investigating the influence of the frequency of applied field could yield interesting results.

While the presented scheme yields encouraging results and invites us to study further applications, we concede that the process is computationally expensive and cumbersome at times. Hence we intend to explore alternative ways to compute magnetic noise as well.

Acknowledgment

This work was supported by the Deutsche Forschungsgemeinschaft (DFG, German Research Foundation) under project 286471992 (Collaborative Research Centre 1261).

References

[1] P. Hayes et al., "Electrically modulated magnetoelectric AlN/FeCoSiB film composites for DC magnetic field sensing," *J. Phys. D, Appl. Phys.*, vol. 51, no. 35, 2018, Art. no. 354002.

[2] N. Smith and P. Arnett, "White-noise magnetization fluctuations in magnetoresistive heads," *Appl. Phys. Lett.*, vol. 78, no. 10, pp. 1448–1450, Mar. 2001.

[3] N. Smith, "Modeling of thermal magnetization fluctuations in thin-film magnetic devices," *J. Appl. Phys.*, vol. 90, no. 11, pp. 5768–5773, Dec. 2001.

[4] F. Bruckner, M. d'Aquino, C. Serpico, C. Abert, C. Vogler, and D. Suess, "Large scale finite-element simulation of micromagnetic thermal noise," *J. Magn. Magn. Mater.*, vol. 475, pp. 408–414, Apr. 2019.

[5] H. Bittel, "Noise of ferromagnetic materials," *IEEE Trans. Magn.*, vol. MAG-5, no. 3, pp. 359–365, Sep. 1969.

[6] S. Ingvarsson, G. Xiao, S. S. P. Parkin, W. J. Gallagher, G. Grinstein, and R. H. Koch, "Low-frequency magnetic noise in micron-scale magnetic tunnel junctions," *Phys. Rev. Lett.*, vol. 85, no. 15, p. 3289, Oct. 2000.

[7] D. Spasojević, S. Bukvić, S. Milošević, and H. E. Stanley, "Barkhausen noise: Elementary signals, power laws, and scaling relations," *Phys. Rev. E, Stat. Phys. Plasmas Fluids Relat. Interdiscip. Top.*, vol. 54, no. 3, p. 2531, 1996.

[8] C. Miehe, "A multi-field incremental variational framework for gradient-extended standard dissipative solids," *J. Mech. Phys. Solids*, vol. 59, no. 4, pp. 898–923, Apr. 2011.

[9] C. Miehe and G. Ethiraj, "A geometrically consistent incremental variational formulation for phase field models in micromagnetics," *Comput. Methods Appl. Mech. Eng.*, vols. 245–246, pp. 331–347, Oct. 2012.

[10] D. Lewis and N. Nigam, "Geometric integration on spheres and some interesting applications," *J. Comput. Appl. Math.*, vol. 151, no. 1, pp. 141–170, Feb. 2003.

[11] C. Miehe, "Strain-driven homogenization of inelastic microstructures and composites based on an incremental variational formulation," *Int. J. Numer. Methods Eng.*, vol. 55, no. 11, pp. 1285–1322, 2002.

[12] R. L. Taylor. (2020). *FEAP—A Finite Element Analysis Program*. [Online]. Available: http://projects.ce.berkeley.edu/feap/

[13] S. Balay, W. D. Gropp, L. C. McInnes, and B. F. Smith, "Efficient management of parallelism in object-oriented numerical software libraries," in *Modern Software Tools for Scientific Computing*, E. Arge, A. M. Bruaset, and H. P. Langtangen, Eds. Basel, Switzerland: Birkhäuser Press, 1997, pp. 163–202.

[14] M. A. Carlton and J. L. Devore, *Probability With Applications in Engineering, Science, and Technology*. Cham, Switzerland: Springer, 2017, pp. 563–575.

[15] G. S. Abo, Y.-K. Hong, J. Park, J. Lee, W. Lee, and B.-C. Choi, "Definition of magnetic exchange length," *IEEE Trans. Magn.*, vol. 49, no. 8, pp. 4937–4939, Aug. 2013.